Tonometric Multi-Wavelength Photoplethysmography for Studying the Cutaneous Microvasculature of the Fingertip

Jukka-Pekka Sirkiä, Tuukka Panula, Matti Kaisti

***Abstract*—Microcirculation is a key compartment in the human cardiovascular system due to its vital roles in providing oxygen and nutrients to tissue, removing metabolic byproducts and regulating blood flow in organs. This network of small blood vessels, known as microvasculature, has been shown to have a link to many cardiovascular diseases. This work presents a method capable of extracting information from different depths of the cutaneous vasculature, including the microvasculature, of the fingertip using an optical sensor with controllable external compression force. Our experiments show that the optical channels can be used to estimate blood pressure at different depths of the tissue, including shallow depths with microvascular blood vessels. Additionally, we show that shorter-wavelength optical signals (465 nm, 515 nm and 590 nm) are more sensitive to pressure-induced vasodilation than longer-wavelength (640 nm and 880 nm) signals. The results indicate that the method can obtain signals originating from different depths of the cutaneous vasculature, from large arteries deep in the skin to arterioles and capillaries close to the surface of the skin. The experimental results are discussed with the help of a Monte Carlo model that simulates photon propagation in tissue under different compression scenarios.**

***Index Terms*—Photoplethysmography, microvasculature, microcirculation, blood pressure, vasodilation.**

I. Introduction

MICROCIRCULATION is often regarded as the most important compartment of the cardiovascular system [1] because of its vital roles in providing nutrients and oxygen to tissue, removing metabolic byproducts from tissue and regulating blood flow in organs [2]–[4]. Numerous studies have investigated the link between cutaneous microcirculation and cardiovascular diseases (CVDs) [5]–[8] and there is mounting evidence showing that cutaneous microcirculation is impaired in many CVDs [9]. The list of conditions related to microvascular dysfunction is long and varied, including ischemic cardiomyopathy, diabetes mellitus, heart failure, obesity, and hypertension [3].

Microvasculature is the terminal vascular network of the systemic circulation consisting of arterioles, capillaries, and venules [1]. In capillaries, molecules between blood and tissue are exchanged, whereas arterioles and venules have key functions in maintaining adequate tissue perfusion [4]. The perfusion is controlled by adjusting the vascular tone in the arterioles, and subsequently the vascular resistance [3]. The arterioles are a major resistive compartment in the microcirculation [4] which is a result of a high wall thickness to lumen diameter ratio [2]. The resistivity of the arterioles also means that the largest blood pressure (BP) drop in the vascular tree occurs in the arterioles [2].

Currently used methods to assess peripheral microvasculature include laser Doppler flowmetry (LDF), forearm plethysmography, and finger plethysmography [10]. LDF measures relative changes in the cutaneous microcirculation by detecting the Doppler shift of a laser light as the light backscatters from moving red blood cells, capable of providing information on endothelial function when combined with endothelial stimuli such as drugs or temperature [11]. Forearm plethysmography is used to assess microvascular function by measuring changes in forearm blood flow during a series of brachial cuff inflations and vasoactive drug infusions [12]. Finger plethysmography measures the reactive hyperaemia index (RHI), which is related to endothelial function, using peripheral artery tonometry where finger pulsations are sensed with a pneumatic probe while the blood flow to the arm is controlled with an upper arm pressure cuff [13]. All of these methods have a common limitation in terms of depth-resolution, as they generate a single signal representing the microvascular function. However, it is important to note that different microvascular blood vessels have different physiological functions. More detailed methods targeting the layer of the skin with capillaries include videocapillaroscopy, where skin capillary patterns are observed with a combination of a microscope and a video camera, and laser speckle contrast imaging, where speckle analysis is used to produce a blood flow index similar to LDF but with significantly shallower skin penetration depth ability [11].

We present a method for studying the cutaneous vasculature of the fingertip by extending the capabilities of photoplethysmography (PPG) to record several signals simultaneously from various depths of the tissue, thus enabling the probing of different tissue layers with distinct vascular properties. We sought to answer whether different wavelengths of light can obtain hemodynamic information from different parts of the vasculature by altering the state of blood vessels with controllable and measurable external pressure. Accordingly, we developed a tonometric multi-wavelength photoplethysmography (MWPPG) device with an integrated pressure generating and sensing system for the measurement of microvascular hemodynamics.

This work involved human subjects or animals in its research. Approval of all ethical and experimental procedures and protocols was granted by Ethical Committee of the Hospital District of Southwest Finland and National Supervisory Authority for Welfare and Health (project number 1574/31/2018).

The authors are with the Department of Computing, University of Turku, Finland (e-mail: jpsirk@utu.fi, mkaist@utu.fi).

The device combines two principles: (i) external compression force exerted on a fingertip alters the underlying vasculature leading to a well-known oscillometric response (used by digital cuff-based BP monitors), and (ii) the penetration depth of light into tissue is wavelength-dependent. Our research group has previously demonstrated (i) with a similar type of tono-oscillometric fingertip device, showing that mean arterial pressure (MAP) together with systolic and diastolic blood pressures (SBP and DBP, respectively) can be accurately measured [14]. The integrated pressure sensor of the developed device measures changes in the arterial segment through volume-pressure coupling. Maximum pulsation occurs near the MAP, that is, at zero transmural pressure P_t defined as: $P_t = P_a - P_e$, where P_a is the pressure inside the artery and P_e is the external pressure [15]. SBP and DBP can then be estimated from the oscillogram using algorithms [14].

Oscillometric responses have been demonstrated also with a finger cuff-based infrared PPG system already in the 1980s [16]. PPG is a technique used to measure blood volume variations (BVVs) in tissue [17], and in a typical setup the skin is illuminated with light while simultaneously the photons reflected from the tissue are registered with a photosensitive device. The PPG signal is produced by variations in the amount of light-absorbing blood in the vascular bed due to cardiac activity. An extension to the standard PPG technique is MWPPG in which tissue is simultaneously probed with several different wavelengths of light. Importantly, these wavelengths penetrate tissue into different depths because optical characteristics (e.g., scattering and absorption coefficients) of skin components (e.g., hemoglobin and melanin) are depended on the wavelength. Thus, different wavelengths of light can probe the cutaneous vasculature at different depths, with longer wavelengths generally penetrating deeper into the tissue [18]. MWPPG sensors have previously been shown to record oscillometric responses in [19] and by our research team [20]. In [19] the main focus was on the use of blue light to measure capillary BP, while [20] focused on examining the effects of external pressure on MWPPG. This article extends previous works by showing that the integration of the two principles, (i) and (ii), results in a new method that unlocks the ability to measure depth-resolved tissue hemodynamics.

The methods section describes the developed device, the experiments performed, the signal processing steps, and the Monte Carlo (MC) model used to gain insight into the results. The method is then demonstrated in two different measurement setups: (i) oscillometric measurements where the external pressure is gradually increased to extract BP readings and (ii) static external pressure measurements where the external pressure is increased near the MAP and kept there for two minutes to observe vasomotor activity.

II. Methods

A. Device

The developed device consists of a printed circuit board (PCB) containing the light-emitting diodes (LEDs) and the photodiode (i.e., the MWPPG sensor, sampling frequency of 500 Hz), a driver PCB containing a system on a chip (SoC) with required peripherals and processing capabilities, pressure sensor (sampling frequency of 100 Hz) PCB, and a stepper motor generating the compression force with an accompanying driver PCB. The SoC is connected via a serial connection to a laptop that runs custom software for interacting with the device. The hardware and software of the developed device have been detailed in the Appendix. The MWPPG sensor PCB and its driver PCB were designed using the Autodesk Eagle 9.5.1 PCB design software. The firmware of the SoC was programmed using the C programming language. The mechanical design was created with the Autodesk Inventor Professional 2021 computer-aided design (CAD) software and the parts were manufactured with a Creality CR-20 Pro fused filament fabrication (FFF) 3D printer. Everything was done in-house except the manufacturing of the PCBs, which was outsourced. A photo of the device is shown in Fig. 1(a) and detailed in Fig. 1(b), Fig. 1(c).

B. Experiments

Oscillometric measurements were performed on ten volunteers (mean age 45 $\pm$ 19 years, range [29, 85] years), of whom five were women. Three oscillometric measurements, where the external pressure on the fingertip was slowly increased approximately 40–50 mmHg above the SBP were taken from each participant in supine position. Three measurements were omitted due to bad measurement quality (bad placement of the fingertip) resulting in a total of 27 oscillometric measurements. Reference BP measurements were taken with Omron M3 (HEM-7154-E) from the upper arm. The reference SBP and DBP readings were converted into MAP using the typical formula of: $MAP = 1/3SBP + 2/3DBP$ [21].

Measurements studying the effects of vasomotor activity were taken from 19 subjects (mean age 58 $\pm$ 19 years, range [29, 84] years), of whom four were women. A measurement in which the external pressure was raised slightly below the MAP and held there for about two minutes was taken from each subject in supine position. The total number of measurements was, therefore, 19.

The measurements were conducted according to the Declaration of Helsinki guidelines with the permission of the Ethics Committee of the Hospital District of Southwest Finland and National Supervisory Authority for Welfare and Health (project number 1574/31/2018). Informed consent was obtained from all participants.

C. Signal Processing

Pressure sensor readings in Pascals were converted into millimeters of mercury (mmHg) by subtracting the baseline pressure (the pressure reading without any load on the piston) from the readings and then dividing by 133.322. All signals were resampled to the same sampling frequency of 500 Hz. The raw signals, both pressure and optical, were filtered with zero-phase fourth-order Butterworth filters to extract the AC and DC components. The AC component was extracted with a band-pass filter with cutoff frequencies set at 0.5 Hz and 8 Hz, while the DC component was extracted with a low-pass filter with a cutoff frequency set at 0.2 Hz. The oscillogram

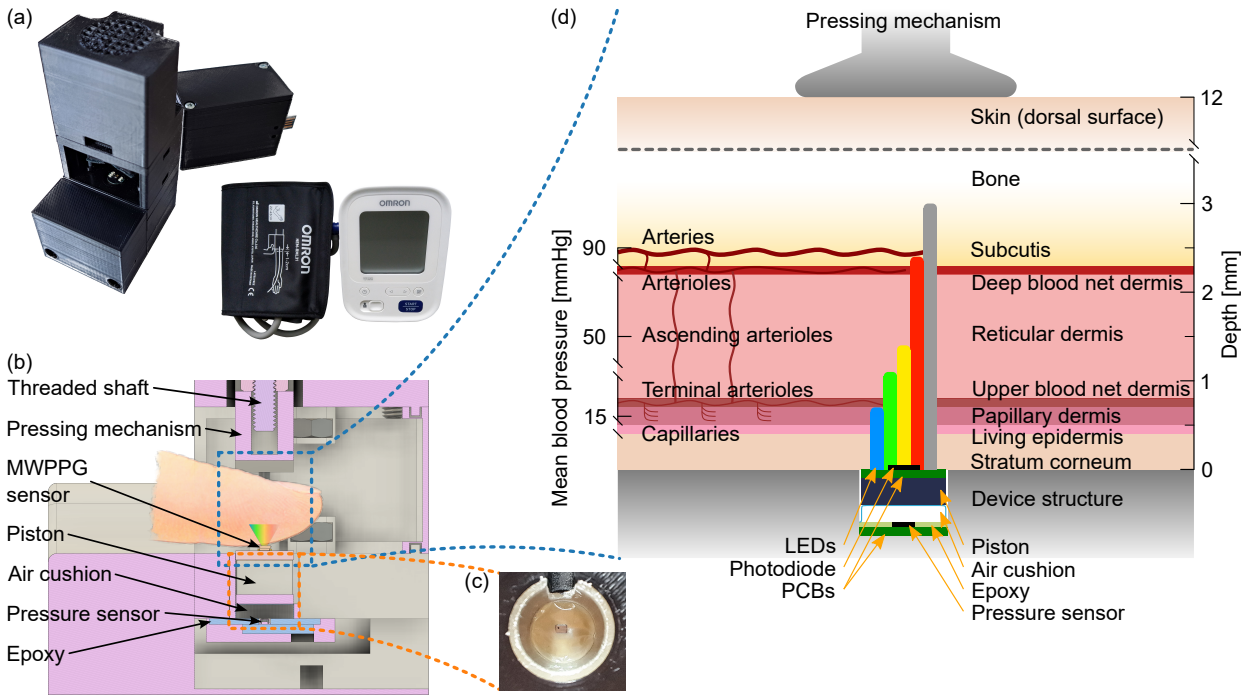

Fig. 1: Concept of the developed method and device. (a) The developed device is shown in the upper left corner. The finger press is shown at the forefront, whereas the box behind contains most of the electronics. The reference arm cuff device (Omron M3) is shown in the lower right corner. (b) Cross-sectional view of the developed device showing the placement of fingertip and the parts of the device. A fingertip is placed on top of a stacked structure consisting of a printed circuit board (PCB) with an optical sensor, a piston capable of moving vertically with minimal friction, and an air cushion that couples pressure information to a barometric pressure sensor fixed to a mechanical housing at the bottom of the chamber. The pressing mechanism at the top of the chamber is controlled using a threaded shaft connected to a stepper motor allowing gradual increase of the compression force. (c) A close-up photo of the air cushion at the bottom of the piston shaft. The metal cover of the pressure sensor can be seen in the middle of the photo. (d) Cross-sectional view of the assumed skin model in the MC simulations. The colored bars represent the different LEDs used in the optical sensor, from blue (left) to infrared (right). The heights of the bars correspond to the mean simulated penetration depths.

was extracted by computing the amplitude envelope of the AC component using the Hilbert transform and then fitting a 13-order polynomial to the peaks of the envelope. To avoid poor fittings, each signal was manually inspected to identify the beginning and the end of the oscillogram. The beginning was defined as the point where the pressure signal started to increase, indicating a contact between the piston and the fingertip, and the end as the point where the oscillogram started to show signs of total occlusion, i.e. no clear PPG waveforms or insignificant amplitudes. Pulse waveform feet, i.e. the onsets or waveform beginnings, and systolic peaks were identified with the automatic multiscale-based peak detection algorithm [22]. The BP readings reported in this study were computed by finding the external pressure level (from the DC component of the pressure signals) at which the envelope fit reached its maximum.

In the measurements studying vasomotor activity, the AC and DC components were computed in the same way as in the oscillometric measurements. The same peak-finding algorithm was also used to identify the pulse waveform feet and systolic peaks (for computing the waveform amplitudes by subtracting the feet from the peaks). The systolic peaks were matched with the feet by finding the closest systolic peak within a 0.4-second interval from a foot. If no systolic peak was found, the foot was omitted. The waveform amplitude time series was computed by averaging the amplitudes over 1-second long intervals. Both the DC component and the waveform amplitude changes were calculated relative to the respective mean values calculated over a 5-second period from the beginning of the 2-minute static pressure holdout. The 95% confidence intervals were calculated as *mean* $\pm$ 1.96 * *standard error*.

D. Monte Carlo Simulation Model

Photon propagation in tissue was simulated with an MC model to gain insight into the interaction of light in tissue. More specifically, we studied penetration depths and light absorption in the different tissue layers presented in the Fig. 1(d), under increasing external compression force. The tissue layers together with the assumed blood vessels in them are based on the organization of the cutaneous microcirculation. In the cutaneous microcirculation arterioles extend from large arteries deep in the subcutaneous tissue and together with venules they form two horizontal plexuses: a deep plexus at the junction of dermis and subcutaneous tissue and a

superficial plexus in the upper parts of the dermis. The two plexuses are connected by ascending arterioles and descending venules. The terminal arterioles of the superficial plexus lead to capillary loops with descending limbs connecting to post-capillary venules of the same plexus. [23] In short, cutaneous blood vessels change from blood-conducting arteries deep in the skin to pressure-regulating arterioles and finally to surrounding tissue maintaining capillaries close to the surface of the skin.

We designed a set of scenarios to simulate the interplay of light and the tissue organization presented in the Fig. 1(d) during an oscillometric measurement where the external compression force steadily increases. The simulation scenarios were constructed based on the notion that under external compression force the smaller, low-pressure, blood vessels in the layers closer to the surface of the skin occlude earlier than the larger, high-pressure, blood vessels in the deeper layers. Therefore, removing blood from a tissue layer works as a simplification for occluding the blood vessels within the specific layer. The scenarios are, hence, snapshots of an oscillometric measurement. The simulation model was run with six scenarios:

- A the base scenario where the contact pressure of the MWPPG sensor is zero;
- B occlusion of the papillary layer;
- C occlusion of the papillary and upper blood net layers;
- D occlusion of the upper half reticular dermis and the layers closer to the surface of the skin;
- E full occlusion of the reticular dermis and the layers before it; and
- F occlusion of the deep blood net layer and the layers before it.

The rules for MC-based photon migration in absorbing and scattering tissues have been well established [24]–[26]. The simulation is based on defining the dimensions and optical characteristics of a tissue model, launching a large number of photon packets (here between 10^7–10^8) one-by-one into the tissue model, and tracking the packets thereafter. Each photon packet follows a random walk process affected by the optical characteristics of the tissue: scattering and absorption coefficients, anisotropy factors, and refraction indices. Only refraction indices are here assumed to be the same for all wavelengths while the rest are assumed to be wavelength-depended. The trajectory of the photon packet is altered by scattering events while absorption events decrease the chances of propagating further by decreasing the photon packet's weight. At the interface of two tissue layers with mismatched refractive indices, the photon packet changes direction, and it can either reflect or transmit. Tracking the photon packet terminates either due to absorption or transmission out of the tissue. These rules of MC simulation are applied here to a tissue model based on volumetric pixels called voxels [27], [28], as the voxels-based approach allows to consider tissue models with rather complex shapes and tissue properties. Details of the used simulation and tissue models have further been discussed in the Appendix.

The MC model was programmed in Python, and to speed up the simulations, the Python functions were translated into efficient processor-optimized machine code using the Numba compiler and parallelized to utilize all logical processors of the central processing unit. The simulations were run on a laptop with an Intel Core i7-11850H CPU and 32 GB of random access memory.

III. Results

A. Multimodal Sensory System for Probing the Cutaneous Vasculature

The developed system comprises a multi-spectral optical sensor, a pressure sensor, and a mechanism to control the external compression force exerted on the fingertip, as detailed in Fig. 1. A measurement is taken by placing a fingertip, with a piece of double-sided tape on the dorsal side, inside a measurement chamber. The volar part of the finger pulp is then adjusted to a good position based on the incoming signals. The ideal position for the piston is below the distal transverse palmar arch, which provides good coupling of the blood vessels and the piston, and hence to the pressure sensor below it. Overall, fingertip, considering the multiple different locations of the hand, has been demonstrated to provide the most consistent BP readings with the upper arm due to its similar bone-to-tissue volume ratio with the upper arm [29]. Once a good position has been found, the fingertip is gently lifted against the pressing mechanism above so that the tape on the dorsal side sticks. The purpose of the double-sided tape is to prevent accidental or subconscious pressing of the piston, which makes it difficult to accurately measure low pressure readings. The pressing mechanism is then lowered, causing the fingertip to press against the piston, which compresses the underlying air chamber. The increase in compression force squeezes the fingertip against the piston and its surrounding area, resulting in the well-known oscillometric response. The recorded pressure is the result of the external compression force and the force of the pulsating blood vessels exerting on the piston. At the same time, the MWPPG probe records signals at all five wavelengths of light, enabling the device to record BVVs and pressure changes simultaneously.

The developed system has five LEDs with wavelengths ranging from shorter-end visible light to NIR: 465 nm (blue), 515 nm (green), 590 nm (yellow), 640 nm (red), and 880 nm (infrared). Differences in the penetration depths of these wavelengths are illustrated in Fig. 1(d). The shorter wavelengths probe mainly the small, low-pressure, capillaries and arterioles, while the longer wavelengths probe all the way down to the large, high-pressure, arteries. The simultaneously increasing external pressure causes the blood vessels to flatten and eventually collapse, starting from the smaller, low-pressure, blood vessels close to the surface of the skin. Thus, the BVVs (oscillometric responses) registered with the different wavelengths of light measure the state of the different blood vessels. Details of the developed hardware and software have been discussed in the Appendix.

B. Light-Tissue Interaction Model

The MC simulation results clearly show differences in penetration ability. Fig. 2(a) shows spatial sensitivity profiles

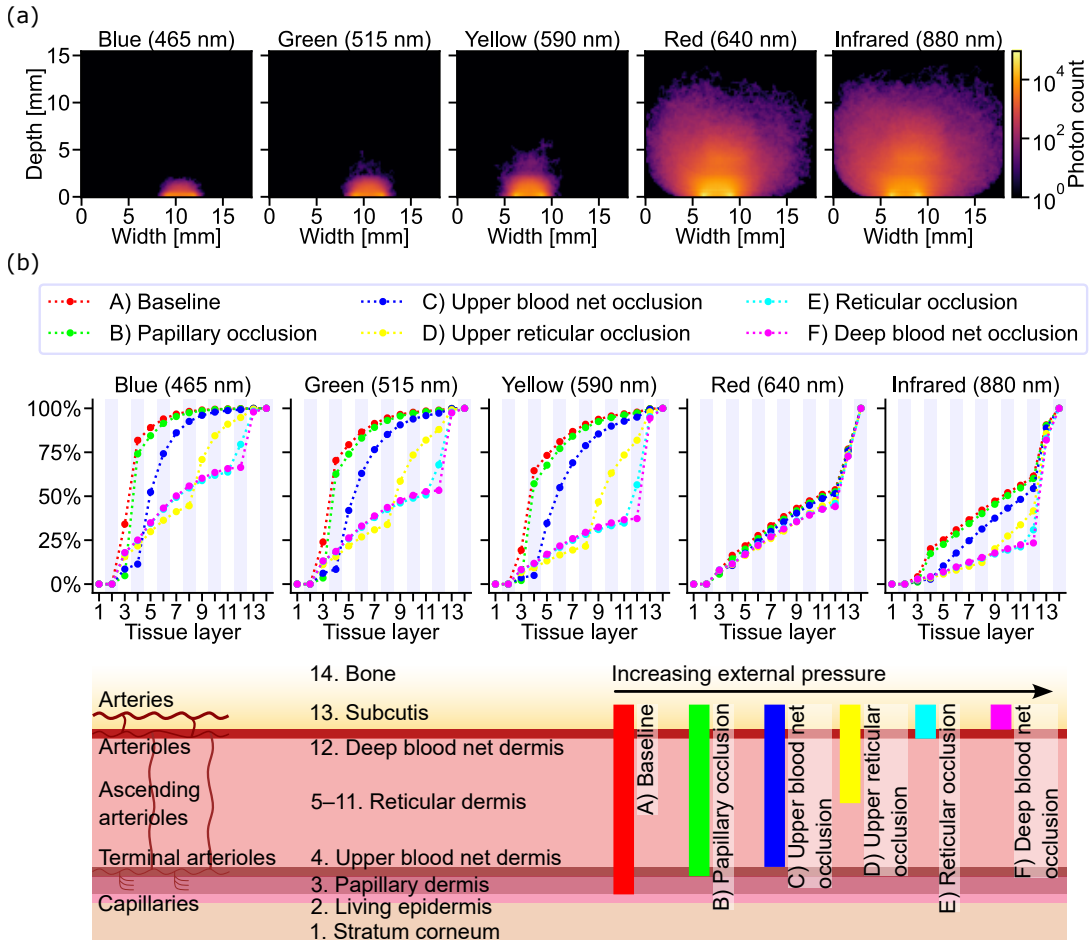

Fig. 2: MC simulation results. (a) Spatial sensitivity profiles showing the simulated photon paths that ended in the photodiode. The penetration depths increase with the wavelength: blue light penetrates only shallowly, whereas infrared light penetrates very deeply. (b) Cumulative layer-wise absorption distributions in each simulation scenario. The tissue layers on the horizontal axes have been marked in the condensed version of Fig. 1(d) shown below the distributions. The reticular layer is thick which is why it was divided into seven sublayers to gain better resolution. Absorption for the first two layers (1 & 2), i.e. epidermis, was ignored because the living epidermis has high absorption due to melanin, making visualizations difficult, but more importantly, the layers do not contain any blood in any scenario – here we are only interested in the layers containing blood since they contribute to the pulsatile AC component of a PPG signal. The vertical colored bars in the tissue model visualize the layers containing blood in each scenario. As an example, in the baseline scenario approximately 82% of the blue channel's simulated photon packet energy in layers 2–13 is absorbed by layer 4.

of the simulated photon paths that ended in the photodiode in the scenario A. Blue light probes the tissue shallowly, whereas infrared light interacts strongly with all tissue layers. Fig. 2(b) presents cumulative absorption distributions as a function of the tissue layer, ignoring the epidermal layers that do not contain any blood. The clearest observation is that the red channel shows smaller changes than the infrared channel. This difference is explained by the red channel's lower blood absorption coefficient: oxygenated hemoglobin, which is abundant in blood with 98% oxygen saturation assumed in the simulations, absorbs more infrared light than red light. As the occlusion propagates and the blood is removed from the tissue layers, the infrared channel shows higher absorption in the deeper layers. However, both channels are heavily affected by absorption in the deeper layers with large arterioles and arteries, and thus effectively probe tissue similarly.

The shorter-end of the spectrum, the blue, green, and yellow channels, shows greater differences between the scenarios than the longer-end of the spectrum. All of the channels have high absorption in the layers containing capillaries and small arterioles in the baseline and papillary occlusion scenarios. Even in the scenario (C) the channels show similar distributions with the deeper layers having somewhat larger contributions at longer wavelengths. However, larger differences start to occur in the scenario (D) where the yellow channel shows the largest changes: the absorption is now heavily affected by the deeper tissue layers. In the scenario (E) the yellow channel actually has a larger contribution from the deeper tissue layers than the red channel. In conclusion, the three shorter-wavelength channels probe the smaller blood vessels close to the surface of the skin at low external compression pressure levels but start to probe deeper, larger blood vessels as the increasing

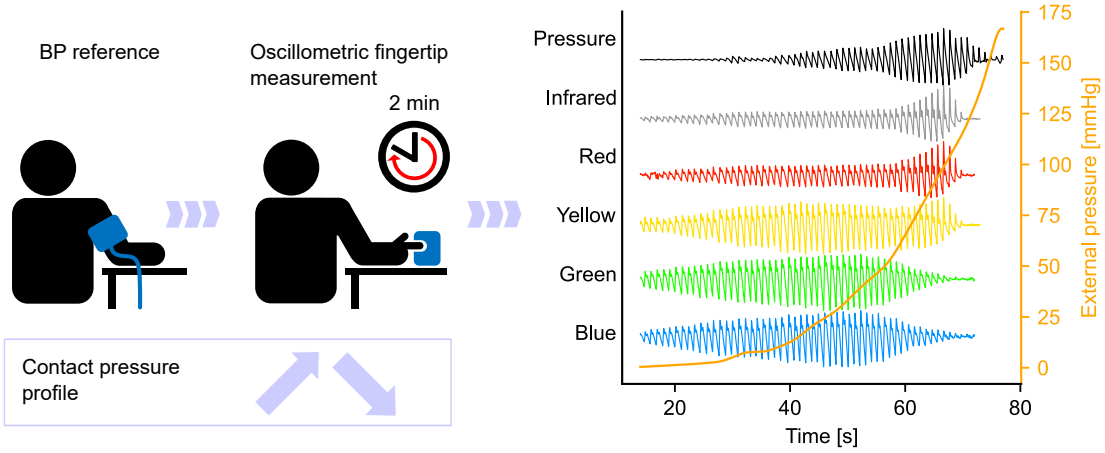

Fig. 3: Tono-oscillometric measurement. Reference BP readings are obtained at the beginning of a measurement using a brachial cuff BP monitor. A pressure ramp-up is then performed on the fingertip using the developed device while recording all six data channels. The recorded signals are post-processed to extract the oscillograms. The signals presented in the figure are the AC components (normalized into range [0, 1]) extracted from an example measurement using a band-pass filter. The PPG signals have also been flipped. The amplitudes show clear responses to increasing external pressure, and importantly, the responses differ between the channels.

external compression pressure pushes the blood out of the shallow tissue layers.

C. Maximum Oscillometric Pressure

Oscillometric measurements were performed to determine the level of external pressure at which the maximum pressure and volume oscillations occur. Traditional oscillometry measures the MAP of the large arteries whereas the presented method specifically extends oscillometric capabilities to measure pressure in several tissue layers. For this reason, we introduce a more general term, maximum oscillometric pressure (MOP), to refer to any measured pressure using oscillometry.

Fig. 3 shows the measurement steps and an example measurement showing oscillograms for the six data channels. Fig. 4(a) shows the pipeline for extracting MOPs from the recorded signals using a combination of: 1) band-pass filtering (and flipping of the PPG signals), 2) Hilbert transformation, 3) peak detection, 4) polynomial fitting and 5) relating the maximum of the polynomial fitting to the low-pass filtered pressure signal. The results of applying this pipeline have been illustrated in Fig. 4(b) showing separate polynomial fittings for each of the five optical channels and the pressure channel presented in the example measurement in the Fig. 3. The red- and infrared-channel MOPs are closely aligned with that of the pressure channel and thus correspond closely to the MAP. The correspondence of these MOPs is also evident in the correlation plots in Fig. 4(c), where the Pearson correlation coefficients for the channel pairs of infrared & pressure and red & infrared are very high (0.934 and 0.994). The high correlation coefficients tell that all three channels probe the tissue in the same way. The correlation and Bland-Altman plots between the pressure channel and the reference device (Omron M3) are also shown in the Fig. 4(c). The developed system is in good agreement with the reference device.

Fig. 4(d) shows box plots along with mean values for each channel, computed over each participants mean MOPs. The figure provides further evidence about the similarity of the red, infrared and pressure channels. Notably, however, the MOPs decrease with decreasing wavelength, and thus penetration depth: from between 80–90 mmHg for the longer-wavelength channels, the pressure channel and the reference device to about 60 mmHg for the yellow channel before reaching approximately 34 mmHg and 30 mmHg for the green and blue channels, respectively. These results indicate a capability to measure the pressure of the superficial tissue layers with smaller, lower-pressure, blood vessels.

The range of variation is quite similar for the red, infrared and pressure channels and the reference device. The shorter-wavelength channels, however, show markedly larger variations with the yellow channel having by far the widest distribution. The reason for this is actually demonstrated in the Fig. 4(b) which shows a typical case where the yellow channel has a two-peak oscillogram. Typically, the first peak is aligned quite closely with the shorter-wavelength channels whereas the latter peak is aligned with the longer-wavelength channels, indicating that at low compression force the yellow channel probes mostly the surface of the skin and at higher level of compression the probing depth increases towards the arteries deeper in the skin. The blue and green channels clearly have better reproducibility compared to the yellow channel.

D. Pressure-Induced Vasodilation

The effect of pressure-induced vasodilation (PIV) was studied in measurements where the external pressure was rapidly raised (on average 3.7 mmHg/s) slightly below the MAP, with the aim of still having pulsations in the blue channel, and held there for a bit over two minutes. The measurement protocol has been illustrated in Fig. 5(a). We examined both the DC components and the pulse waveform amplitudes of the AC

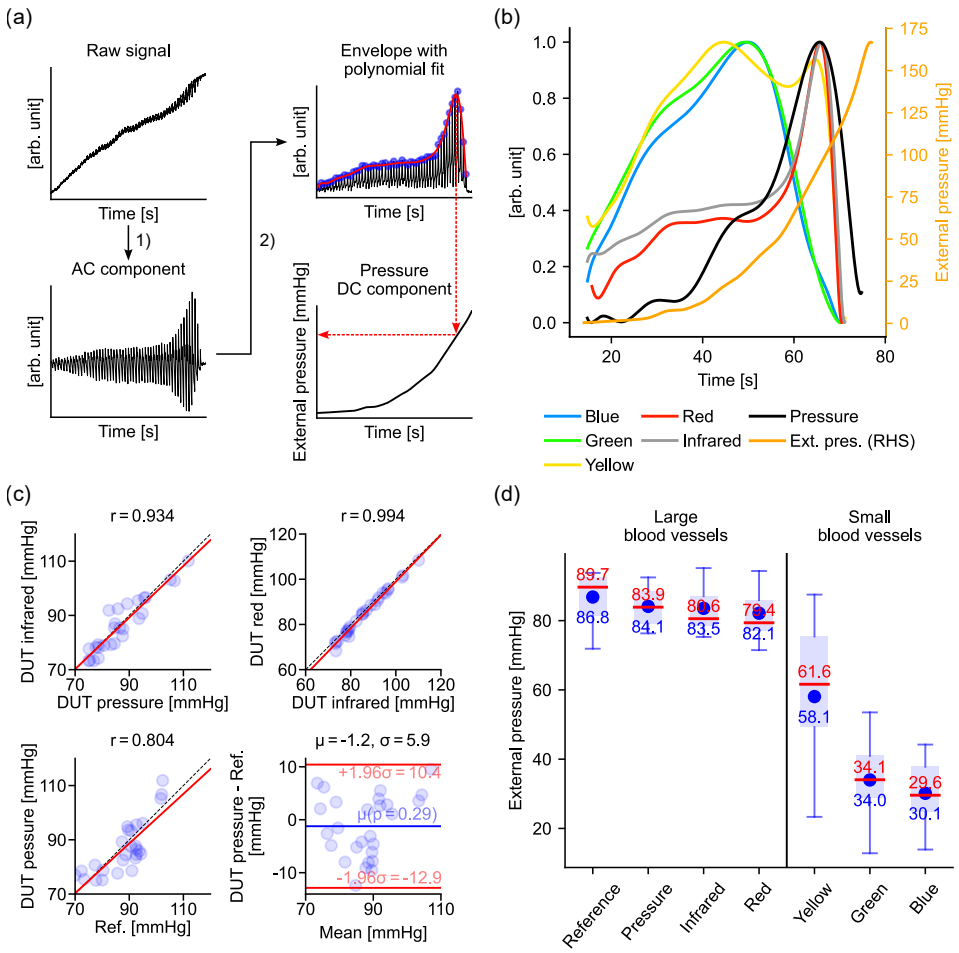

Fig. 4: Experimental MOP results. The term *pressure* refers to the pressure channel (similarly as *infrared* to infrared channel) whereas the term *external pressure* refers to the measured external pressure. (a) Pipeline for extracting a MOP from a raw signal. 1) Band-pass filter the raw signal to extract the AC component. Flip the signal if it is a PPG signal to obtain waveforms where the systolic peaks are local maxima. 2) Perform Hilbert transformation to obtain the envelope and find the envelope peaks. Compute a polynomial fit on the found peaks. Finally, find the external pressure reading at which the polynomial fit maximum occurs. (b) Normalized oscillogram envelopes for the five optical channels and the pressure channel presented in the example measurement in the Fig. 3. (c) Correlation plots for the pairs of infrared & pressure, red & infrared, and developed device (abbreviated as DUT, i.e. device under test, in the figure) pressure & reference device (abbreviated as Ref. in the figure) pressure. All of the pairs show strong correlation. The Bland-Altman plot shows that the developed device is in good agreement with the reference device. (d) Box plots showing the reference device MOP together with the MOPs of the six data channels of the developed device. The median and mean values have been presented with red and blue colors, respectively. The pressure, infrared, and red channels clearly probe the arterial vasculature, as they are closely in line with each other and the reference device. The shorter-wavelength channels show larger variations and a clear tendency for the mean values to decrease with wavelength of light. One test participant was omitted from the figure for clarity due to high BP readings (SBP/DBP of 138/84 mmHg).

components because both are known to vary due to vasomotor activity [17], [30], [31].

Relative mean changes along with 95% confidence intervals both in DC components and waveform amplitudes during a 2-minute static external pressure period have been provided in Fig. 5(b). Fig. 5(c) summarizes the results as box plots. Negative DC level changes tell that the amount of light detected by the photodiode has decreased because of increased blood volume absorbing more light. Positive waveform amplitude changes on the other hand tell that the blood vessels have become less constricted due to PIV, allowing stronger pulsations. The yellow channel has the largest DC level change, and interestingly, the channels form a V-shaped pattern – the DC level changes get smaller as the wavelength decreases/increases from the yellow channel.

Regarding the pulse waveform amplitudes in the Fig. 5(b) and Fig. 5(c), the blue channel sees the largest increase with a decreasing pattern as the wavelength increases before plateauing at the red channel. The shorter-wavelength channels show greater variance compared to the longer-wavelength

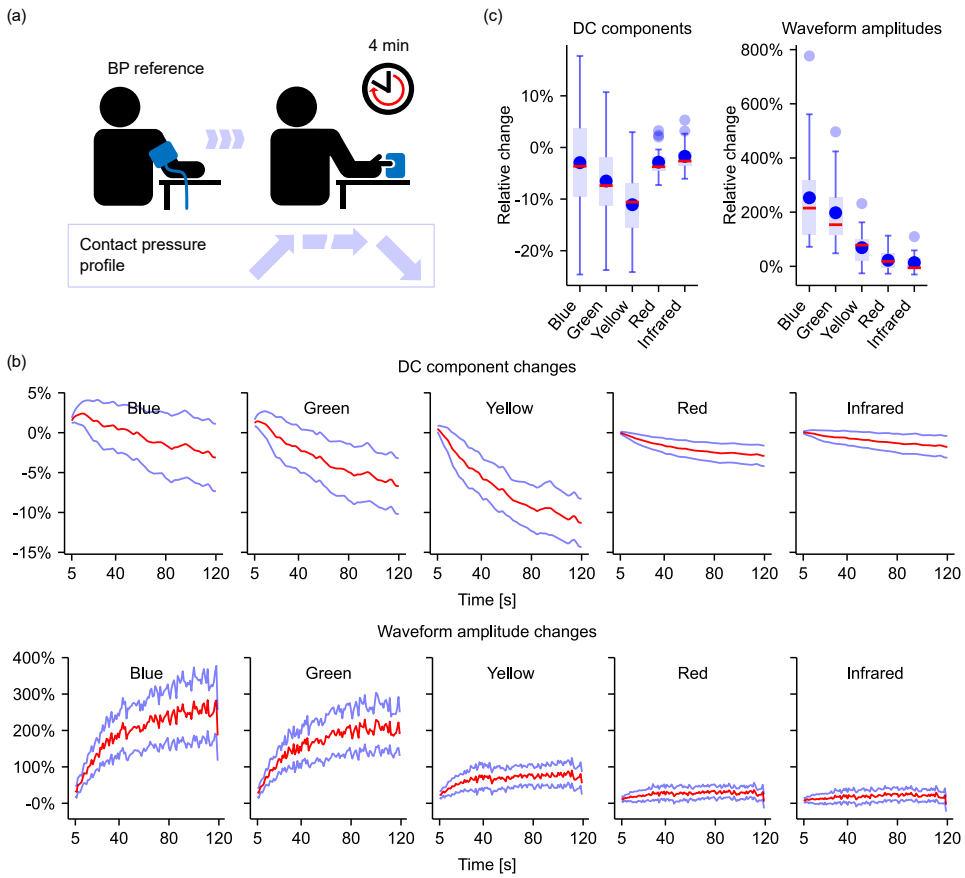

Fig. 5: Results for measurements studying the PIV phenomenon. (a) Steps of the measurement. Similarly to the oscillometric measurement, reference BP readings are obtained at the beginning. Increasing pressure is then applied on the fingertip until the MAP is reached. The external pressure is kept constant for two minutes after which the pressure is released. (b) Mean DC component and waveform amplitude changes together with 95% confidence intervals. The changes have been computed relative to a mean value over a 5-second period from the beginning of the 2-minute static pressure holdout. (c) A figure summarizing the results in the Fig. 5(b). The box plots are based on mean values computed over the last five seconds in the Fig. 5(b). The red lines mark the median values while the blue circles mark the mean values. The greatest DC component change occurs in the yellow channel, while the greatest waveform amplitude change occurs in the blue channel.

channels. This is due to the high external pressure, which causes the shorter-wavelength pulse waveform amplitudes to be initially small, allowing more room for the amplitudes to recover.

IV. Discussion

We developed a tonometric method capable of probing cutaneous vasculature at different depths, from large arteries buried deep in the skin to smaller blood vessels located close to the surface of the skin. The method was demonstrated with two sets of experimental measurements: oscillometric measurements to extract arterial and microvascular BP, and measurements examining vasomotor activity. The experimental results were further corroborated with an MC simulation model.

The strong correlation results (Fig. 4(c)) between the infrared and pressure channels and the agreement of the developed system with the brachial cuff-based reference device agree with the results in [16] where finger-based volume-oscillometric infrared mean pressure was found to closely correlate with the mean brachial intra-arterial pressure ($r = 0.995$ vs. in our results r was 0.934 between the infrared and pressure channels and 0.804 between the pressure channel and the reference device) and our earlier finding of fingertip MAP matching well with that of an arm cuff device ($r = 0.86$, $\mu = -4.0$ mmHg and $\sigma = 5.4$ mmHg vs. $r = 0.80$, $\mu = -1.2$ mmHg, $\sigma = 5.9$ mmHg in the presented results) [14]. The close agreement of the infrared and pressure channels with the reference device is further supported by the results in [32] where an oscillometric finger pressing method using infrared PPG was demonstrated as a potential BP measurement technique. The MC simulation results (Fig. 2) further validate the experimental results by showing that both red and infrared channels measure the deep arterial vasculature. Finger-based volume-oscillometric infrared PPG is, therefore, a surrogate for the typical oscillometric pressure method.

The finding of decreasing MOPs as a function of decreasing wavelength of light in the Fig. 4(d) is in agreement with the general working of the systemic blood circulation, where BP decreases as blood vessels change from the arteries to

arterioles, capillaries, venules and finally to veins [33]. In the arteriolar limb of the capillary loop BP is about 40 mmHg [34] whereas in the capillary it is only about 10–20 mmHg [34]–[37] with pulse pressure approximately below 10 mmHg [35]. These values suggest that the experimentally measured MOPs of the blue and green channels (Fig. 4(d)) are closer to arteriolar BP than capillary BP, indicating a strong arteriolar contribution. The yellow channel has a higher mean value (Fig. 4(d)) that settles between capillary pressure and MAP of the arteries, indicating an even higher arteriolar, and in some measurements also arterial, contribution. Both of these experimental results are in line with the MC simulation results (Fig. 2(b)), which showed a large contribution from tissue layers with arterioles, with contributions increasing with wavelength and external pressure. Nonetheless, the MOP results clearly demonstrate that the penetration depth increases with the wavelength, and that by using different wavelengths of light in oscillometric measurement, information from different depths of the layered cutaneous vasculature, including microvasculature, can be obtained.

The high variation of the yellow channel's MOP results due to two-peak oscillograms is interesting, although expected based on the simulation results. The MC results in Fig. 2(b) showed that the yellow channel has the largest shift in tissue layer probing as the occlusion propagates, shifting from the shallow tissue layers to the deeper tissue layers. Thus, it can be hypothesized that at low external pressure levels the yellow channel probes the maximally pulsating lower-pressure blood vessels causing the first peak and then moves on to probe the large blood vessels deeper in the tissue. Once the external pressure level reaches the MAP of the arteries, i.e. the point of the vessels' maximal pulsation, the second peak is formed. Given that the algorithm finds the maximum of the envelope fit, the reported maximum can be either the first or the second peak, explaining the large variation seen in the MOP results. Therefore, improving the measurement setup and possibly also the algorithm could result in more reliable MOP results for the yellow channel.

The separate measurement set on PIV demonstrated additional capabilities of the method in extracting penetration depth-dependent signals. The simulation results (Fig. 2(b)) show that yellow light is the most representative of the reticular dermis, where arterioles are abundant. Arterioles with smooth muscle cells in the vascular wall are known to mediate vasomotor activity [23]. Therefore, the result that the yellow DC level reacts the strongest to static external pressure is quite expected. Combining this with the results of the waveform amplitude changes, the experimental results imply that increased arteriolar blood volume leads to increased pulsations closer to the surface of the skin. The presence of vasodilation in the measurements is supported by the results in [31] where infrared PPG signal was observed during cold-induced vasoconstriction. Given that vasoconstriction and vasodilation are the opposite effects of vasomotoric activity, the results of increased DC levels and decreased pulse waveform amplitudes in [31] support our results. Furthermore, in [38] skin blood flow measured with LDF was observed to recover shortly after stopping an external pressure increase to maintain constant pressure. Although, the external pressure ramp-up was significantly slower (16.7 Pa/s, approximately 0.13 mmHg/s) and was stopped at a lower pressure level (approximately 30 mmHg), we believe that the phenomena seen in these two datasets are the same considering that PIV occurs at pressure levels below 20 kPa (approximately 150 mmHg) [39], which is significantly higher than the static external pressure maintained in our measurements.

The article introduced a tono-oscillometric approach to the currently evolving MWPPG research [18] and the presented results are encouraging for further development of the method toward a diagnostic tool. The increased resolution in PIV measurements allows to study the effects of vasomotor activity at different depths of the cutaneous vasculature, possibly enabling to develop new indices to measure vasomotor activity. Additional clinical value could be gained, for example, in diabetes monitoring because PIV is known to be impaired among diabetic patients [40], [41] and in identifying patients at risk of pressure ulcers. MWPPG could also add new dimensions to measuring endothelial function, and in particular to RHI measurements, which have already been demonstrated using a single-wavelength (infrared) PPG instead of typical pneumatic probes [42]. Improved resolution in BP measurement, i.e., simultaneous measurement of BP in large and small arteries, could help in hypertension prevention and management considering the cross-link between microcirculation and macrocirculation. In this vicious circle, increased total peripheral resistance (TPR) due to microvascular alterations increases the mean BP, which then again has damaging effects on the microvasculature over time, leading to even more increased TPR and mean BP. [43]

However, unlocking the full potential of the method requires more research to understand the uncertainty in the information content of MWPPG signals, as they contain overlapping information – for example, the infrared channel passes through the same tissue layers as the blue channel. This uncertainty means that MOPs extracted from shorter wavelength channels (below the wavelength of red light) do not necessarily reflect the mean BP of any specific type of blood vessel, as is the case with red and infrared light and arterial BP. Furthermore, the depth origins of the signals can vary due to various factors ranging from ambient temperature (temperature-induced vasoconstriction/vasodilation) to subject-specific things like the size and overall structure of the fingertip. We acknowledge that the results might be device specific to some extent, depended on, for example, the used compression technique (tonometric vs. cuff). To rule out the possibility of the configuration of the MWPPG sensor LEDs affecting the results, motivated by the LED-photodiode distance measurement results in [44], a test was performed in which the distance between the blue LED and the photodiode was halved. The change had a negligible effect on the oscillograms, with the exception that inverted PPG signals, as described in [45], were observed when the fingertip was approaching, moved by the compression mechanism, the photodiode.

We further acknowledge the challenges with respect to finger-based measurement solutions, such as impaired signal quality with cold fingers, which is typical for finger-based PPG

applications. The device is also sensitive to the position of the fingertip, which is why the fingertip has to be carefully positioned. In its presented form the optimal fingertip location was manually decided based on visual inspection of the specific fingertip and moving the fingertip in small increments above the MWPPG sensor while inspecting the real-time signals. In a future version, this could be automated with algorithms to provide automatic positioning guidance to the user. In addition to such engineering related matters, future studies should focus on collecting more data from different age groups and from patients with different diseases (e.g., hypertension, diabetes, and peripheral arterial disease) to further investigate the diagnostic potential of the presented method.

V. Conclusion

We presented a method combining a multi-spectral optical sensor with controllable and measurable external compression force to obtain signals originating from different depths of the cutaneous vasculature. The method was able to extract blood pressure readings from arteries to microvascular blood vessels. The red and infrared channel values aligned closely with those of the pressure signal and the reference device, while the shorter wavelength optical channels showed decreasing pressure readings with decreasing wavelength of light. The effects of pressure-induced vasodilation were studied in measurements with static external pressure. The yellow channel showed the greatest change in DC components, whereas the blue channel had the greatest change in waveform amplitudes, both indicating the presence of vasodilation. The empirical results were supported by Monte Carlo simulation results showing that longer wavelengths of light probe deeper tissue layers with larger blood vessels, and that the probing depth of shorter-wavelength light increases when external pressure pushes blood out from the smaller blood vessels that are closer to the surface of the skin.

Acknowledgment

This work was supported in part by Business Finland, project number 1574/31/2018. The works of J.-P. Sirkiä and T. Panula were partially funded by the University of Turku Graduate School.

Appendix A
Tonometric Multi-Wavelength Photoplethysmography Device

A. Hardware

The custom-made multi-wavelength photoplethysmography (MWPPG) sensor consists of five Kingbright Electronic Co, Ltd. APT series light-emitting diodes (LEDs) emitting light at five different wavelengths: 465 nm (blue), 515 nm (green), 590 nm (yellow), 640 nm (red), and 880 nm (infrared). The wide spectral bandwidth sets a requirement for the spectral sensitivity of the photodiode, since the design has space only for a single photodiode. The size restriction is due to the requirement of an average-sized fingertip to properly cover the full sensor surface area and keep the diameter of the piston as small as possible. The Vishay Semiconductor VEMD1060X01 photodiode was eventually selected due to its spectral bandwidth of 350–1,070 nm (peaking at 820 nm) and small size (surface-mount device package 0805). The LEDs and the photodiode were mounted on a separate circular printed circuit board (PCB) having a diameter of just 9.6 mm.

The aforementioned sensor PCB is driven by another custom-designed PCB through a small connector at the bottom. The driving PCB contains one LED driver for each channel. The LED driving circuits are constant current sink circuits constructed with NPN bipolar junction transistors (BJT) working in emitter follower fashion. The constant current nature of the setup guarantees stable LED light output characteristics. The current control of the LEDs is handled by two Microchip's 4-channel 12-bit MCP4728 digital-to-analog converters, which feed the bases of the BJTs. Next to the LED driving circuits is a transimpedance amplifier circuit responsible for converting the small photodiode current into voltage. The resulting voltage is routed to Analog Devices' 16-bit AD7680 successive approximation analog-to-digital converter. The components are powered by two ultralow-noise, low-dropout linear regulators, of which one provides 4.7 V for the LEDs and the other one 3.3 V for the rest of the components.

The compression force generation is performed in a similar way as in the device presented earlier by our research group in [14], with a unipolar stepper motor (28BYJ-48) driven by transistors in the Darlington configuration. The pressure sensing functionality is also constructed in a manner similar to that of [14] with the only differences being that the pressure sensor was changed to a newer version (BMP280 by Bosch Sensortec) and that the pressure sensor was not modified in any way. Instead of removing the metal cover of the pressure sensor element, the whole sensor PCB was cast in epoxy to make the surrounding area even with the top of the metal cover. A small air cushion was then sealed around the pressure sensor using a piece of double-sided tape with strong adhesion. The double-sided tape proved to be adequate in sealing the air cushion, but to be sure, a gasket made out of rubber was placed around the air cushion, providing additional sealing once the sensor structure was installed at the bottom of the device. The air cushion forms a closed space inside which pressure changes are transmitted to the sensor element through the small hole in the metal cover.

The motor and pressure sensor, along with the MWPPG driving PCB, are connected to Nordic Semiconductor's nRF52840 Dongle, which is a low-cost USB dongle suitable for rapid prototyping. The nRF52840 system on a chip (SoC) includes a 32-bit ARM Cortex-M4 processor running at 64 MHz together with the required digital peripherals such as the serial peripheral interface and the two-wire interface. The system is presented in the form of a block diagram in Fig. 6.

B. Software

The device firmware was written in the C programming language using the Nordic Semiconductor nRF5 software development kit. The firmware is responsible for sampling the MWPPG and pressure sensors while controlling the motor.

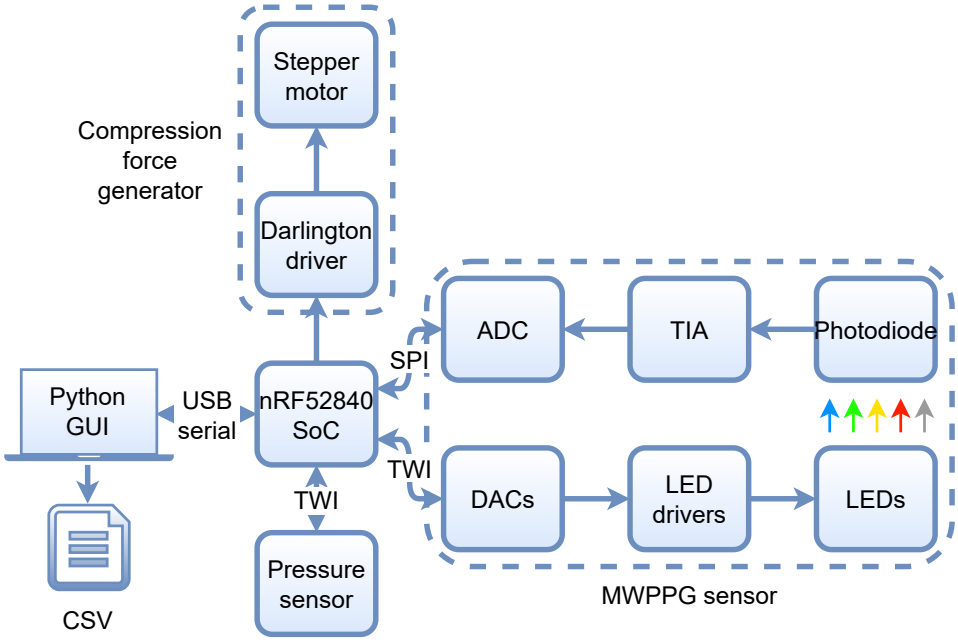

Fig. 6: System block diagram of the developed device.

To guarantee precise sampling, the firmware was built around timer interrupts running on the high-frequency clock of the nRF52840 SoC. The interval between the interrupts defines the sampling frequency. Whenever a timer interrupt occurs for the MWPPG sensor, each one of the LEDs is turned on for a brief moment of time one by one, and the ADC for the photodiode output is read. The recorded data together with a timestamp and an ambient light (i.e., when all of the LEDs are turned off) value are sent over a virtual USB serial port to a computer. A similar read-send process is performed for the pressure sensor. The stepper motor is simultaneously controlled by a timer, and its state is partly connected to the pressure readings in that once a maximum allowed pressure (usually set above the systolic blood pressure) is reached, the stepper motor reverses its direction. The firmware keeps track of the steps taken so that the stepper motor can be returned to its initial starting position. The firmware is controlled over a virtual serial port with a series of bytes that carry commands and data.

The accompanying computer runs an application written in Python. The application has a graphical user interface with real-time graphs for the incoming MWPPG and pressure data, together with control mechanisms to change the device configuration and control the measurement process. The received data are stored as a comma-separated values file and later analyzed with Python scripts.

Appendix B
Monte Carlo Simulation Model

The general equations for propagating photon packets in tissue have been presented in [24]–[26] while the additional requirements for voxel-based tissue model have been presented in [27], [28]. The used Monte Carlo (MC) model was verified against the results found in the literature [24], [26], [27], [46]. The verification results are presented in table I, which shows that the accuracy of the model agrees well with the reference results.

The tissue layers together with their model parameters have been presented in Table II. Layer thicknesses (t) are based on [47], [49] except for the subcutaneous tissue and bone (explained below) and for the stratum corneum. The thickness of the stratum corneum, the outermost layer of the skin, is adapted from [52]–[54] because the epidermal layer of the volar parts, i.e. the friction ridge skin, of the fingertips usually have a thicker epidermal layer than elsewhere in the body [54]. The volume fractions of blood and water (C_b and C_w, respectively) are based on [47]. The melanin concentration (C_m) in the living epidermis for a very fair skin type was estimated from the data in [55]. The refractive indices (n) are based on [47], [49] and were assumed to be wavelength-independent. The mean inner diameters of the blood vessels (d) were roughly approximated based on [23], [56]. Regarding the bone, the refractive index was assumed to be 1.56 [50], while the rest of the parameters were assumed to be zero, except for the thickness which is depended on the shape of the distal phalanx assumed in the study (explained below).

The properties of the wavelength-dependent tissue components have been presented in Table III with the appropriate references for the values. The total absorption coefficient as a function of layer i in Table II and wavelength λ was calculated as [51]:

$$\begin{aligned}\mu_a(i,\lambda) = \alpha(i,\lambda)C^b(i)\mu_a^b(\lambda)+\\ (1-C^b(i)-C^w(i))\mu_a^t(\lambda)+\\ C^m(i)\mu_a^m(\lambda)+C^w(i)\mu_a^w(\lambda),\end{aligned} \tag{1}$$

where α is the correction factor for the fact that blood is not homogeneously distributed in the tissue but instead flows in blood vessels; C^b, C^w, C^m are volume fractions for whole

TABLE I: MC model verification results.

(a) Verification 1. Ten MC simulations of 50,000 photon packets were simulated for the following slab of turbid medium (outside medium $n = 1$), as presented in [26]: $n = 1$, $u_a = 10$ cm^{-1}, $u_s = 90$ cm^{-1}, $g = 0.75$, $t = 0.02$ cm (thickness). The total diffuse reflectance and total transmittance values have been presented as *mean (standard error)*. The values of [24] are from [26] because even though [24] presents similar results the exact parameters used are not as clearly stated as in [26].

Source	Diffuse reflectance	Transmittance
[24], according to [26]	0.09711 (0.00033)	0.66159 (0.00049)
[26]	0.09734 (0.00035)	0.66096 (0.00020)
This study	0.09710 (0.00034)	0.66094 (0.00046)

(b) Verification 2. Ten MC simulations of 5,000 photon packets were simulated for the following semi-infinite turbid medium (outside medium $n = 1$), as presented in [26]: $n = 1.5$, $u_a = 10$ cm^{-1}, $u_s = 90$ cm^{-1}, $g = 0$. The total diffuse reflectance values have been presented as *mean (standard error)*.

Source	Diffuse reflectance
[24] according to [26]	0.26079 (0.00079)
[26]	0.25907 (0.00170)
This study	0.25867 (0.00169)

(c) Verification 3. Five MC simulations of 10,000 photon packets were simulated in the following three-layer slab (outside medium $n = 1$), as presented in [27]: 1 mm of glass ($n = 1.54$, $u_a = 0$ cm^{-1}, $u_s = 0$ cm^{-1}), 0.7 mm of skin ($n = 1.38$, $u_a = 1.36$ cm^{-1}, $u_s = 14.16$ cm^{-1}, $g = 0$), and another 1 mm of glass. The total diffuse reflectance and total transmittance values have been presented as *mean (standard deviation)*.

Source	Diffuse reflectance	Transmittance
[27]	0.2125 (0.0019)	0.4988 (0.0017)
This study	0.20643 (0.0026)	0.51054 (0.0036)

(d) Verification 4. Ten MC simulations of 100,000 photon packets were simulated in a medium consisting of $121\times121\times61$ voxels (voxel side length of 0.1 cm) with the following optical properties: $n = 1.37$, $u_a = 0.1$ cm^{-1}, $u_s = 100$ cm^{-1}, $g = 0.9$ [46]. The total diffuse reflectance and total absorption values have been presented as *mean (standard error)*.

Source	Diffuse reflectance	Absorption
[46]	0.6143 (0.0001)	0.3613 (0.0001)
This study	0.6168 (0.0003)	0.3595 (0.0003)

blood, water and melanin, respectively; μ_a^b, μ_a^t, μ_a^m and μ_a^w are absorption coefficients for whole blood, water- and blood-free tissue, melanin and water. The correction factor is calculated as [51]:

$$\alpha(i,\lambda) = 1/[1 + 1.482(0.5\mu_a^b(\lambda)d(i))^{1.151}], \quad (2)$$

where d is the mean diameter (in mm) of the blood vessels in the layer i. The total scattering coefficient is calculated as [51]:

$$\mu_s(i,\lambda) = \alpha(i,\lambda)C^b(i)\mu_s^b(\lambda) + (1 - C^b(i))\mu_s^t(i,\lambda), \quad (3)$$

where μ_s^b and μ_s^t are the scattering coefficients of whole blood and bloodless tissue (epidermis (μ_s^e)/dermis (μ_s^d)/subcutis (μ_s^s)), respectively. Finally, the anisotropy factor is calculated as [51]:

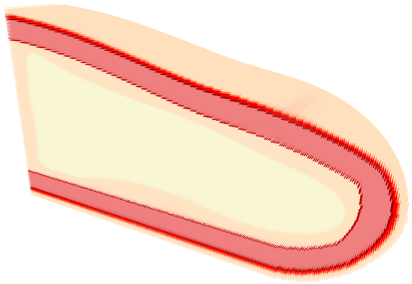

Fig. 7: Cross-sectional view of the voxelized fingertip model.

$$g(i,\lambda) = [\alpha(i,\lambda)C^b(i)\mu_s^b(\lambda)g^b(\lambda) + (1 - C^b(i))\mu_s^t(i,\lambda)g^t(\lambda)]/\mu_s(i,\lambda), \quad (4)$$

where g^b and g^t are the anisotropy factors of whole blood and bloodless tissue. Bone was treated separately using the parameter values μ_a^{bo}, μ_s^{bo}, g^{bo} also presented in the Table III.

The tissue model of the fingertip was based on a photograph of a real fingertip slightly pressed against a smooth surface. The photograph was then turned into a rough 3D model using the Autodesk Inventor Professional 2021 CAD software. The resulting model was then processed with a Python program to fill it with layers representing the different layers of skin tissue. The subcutis was assumed to fill the rest of the fingertip volume once all of the layers above it had been created. A bone model approximating the shape of the distal phalanx, as presented in [56], was then added to the subcutaneous tissue. The size of the bone was approximated to be in line with the rest of the fingertip. Therefore, the resulting model approximates a real fingertip without using advanced imaging solutions, such as magnetic resonance imaging, which would allow for a very detailed model [57]. A cross-sectional view of the voxelized fingertip model has been presented in Fig. 7.

TABLE II: Model parameters specific to tissue layers. Nomenclature for the layers: SC: stratum corneum; LE: living epidermis; PD: papillary dermis; UB: upper blood net dermis; RD: reticular dermis; DB: deep blood net dermis; SU: subcutis. The letter E/D/S in parentheses after the layer abbreviation tells the main skin layer type: E: epidermis; D: dermis; S: subcutis.

Layer	t [mm]	C^b [1]	C^w [1]	C^m [1]	n [1]	d [µm]
SC (E)	0.4	0	0.05	0	1.5	0
LE (E)	0.1	0	0.2	0.03	1.34	0
PD (D)	0.2	0.04	0.5	0	1.4	15
UB (D)	0.1	0.3	0.6	0	1.39	25
RD (D)	1.4	0.05	0.7	0	1.4	40
DB (D)	0.1	0.14	0.7	0	1.38	50
SU (S)	-	0.06	0.65	0	1.44	100

TABLE III: Wavelength-depended model parameters. The parameters μ_a, μ_s and g refer to absorption coefficient ([mm^{-1}]), scattering coefficient ([mm^{-1}]) and anisotropy factor ([1]), respectively.

Parameter	Wavelength [nm]					References
	465	515	590	640	880	
μ_a^m	88.7	62.1	38.7	29.2	9.6	[47]
μ_a^b	19.5	11.3	9.7	0.2	0.6	[48]
μ_a^w	2.5E-5	2.8E-5	1.5E-4	3E-4	5.5E-3	[47]
μ_a^t	0.16	0.12	0.08	0.06	0.02	[49]
μ_a^{bo}	1.1	0.9	0.8	0.4	0.3	[50]
μ_s^b	81.2	84.2	81.7	88.8	71.6	[48]
μ_s^e	29.2	26.2	23.8	22.6	21.8	[50]
μ_s^d	16.8	14.3	11.7	10.5	6.7	[50]
μ_s^s	4.8	4.2	3.7	3.5	2.6	[50]
μ_s^{bo}	27.0	24.3	23.1	22.6	17.7	[50]
g^b	0.96	0.98	0.97	0.98	0.98	[48]
g^t	0.75	0.77	0.79	0.81	0.86	[51]
g^{bo}	0.9	0.9	0.9	0.9	0.9	[50]

REFERENCES

[1] G. Guven, M. P. Hilty, and C. Ince, "Microcirculation: Physiology, pathophysiology, and clinical application," Blood Purification, vol. 49, no. 1-2, pp. 143–150, 2020.

[2] A. S. Popel and P. C. Johnson, "Microcirculation and hemorheology," Annual review of fluid mechanics, vol. 37, pp. 43–69, Jan 2005.

[3] D. D. Gutterman, D. S. Chabowski, A. O. Kadlec, M. J. Durand, J. K. Freed, K. Ait-Aissa, and A. M. Beyer, "The human microcirculation," Circulation Research, vol. 118, no. 1, pp. 157–172, 2016.

[4] C. A. den Uil, E. Klijn, W. Lagrand, J. Brugts, C. Ince, P. Spronk, and M. Simoons, "The microcirculation in health and critical disease," Progress in Cardiovascular Diseases, vol. 51, no. 2, pp. 161–170, 2008.

[5] R. G. IJzerman, R. T. De Jongh, M. A. M. Beijk, M. M. Van Weissenbruch, H. A. Delemarre-van de Waal, E. H. Serné, and C. D. A. Stehouwer, "Individuals at increased coronary heart disease risk are characterized by an impaired microvascular function in skin," European Journal of Clinical Investigation, vol. 33, no. 7, pp. 536–542, 2003.

[6] A. Kruger, J. Stewart, R. Sahityani, E. O'Riordan, C. Thompson, S. Adler, R. Garrick, P. Vallance, and M. Goligorsky, "Laser doppler flowmetry detection of endothelial dysfunction in end-stage renal disease patients: Correlation with cardiovascular risk," Kidney International, vol. 70, no. 1, pp. 157–164, 2006.

[7] R. Yamamoto-Suganuma and Y. Aso, "Relationship between post-occlusive forearm skin reactive hyperaemia and vascular disease in patients with type 2 diabetes—a novel index for detecting micro- and macrovascular dysfunction using laser doppler flowmetry," Diabetic Medicine, vol. 26, no. 1, pp. 83–88, 2009.

[8] S. C. Agarwal, J. Allen, A. Murray, and I. F. Purcell, "Laser Doppler assessment of dermal circulatory changes in people with coronary artery disease," Microvascular Research, vol. 84, no. 1, pp. 55–59, Jul. 2012.

[9] M. Hellmann, M. Roustit, and J.-L. Cracowski, "Skin microvascular endothelial function as a biomarker in cardiovascular diseases?" Pharmacological Reports, vol. 67, no. 4, pp. 803–810, 2015, perspectives in Pharmacology of Endothelium: From Bench to Bedside.

[10] S. Masi, D. Rizzoni, S. Taddei, R. J. Widmer, A. C. Montezano, T. F. Lüscher, E. L. Schiffrin, R. M. Touyz, F. Paneni, A. Lerman, G. A. Lanza, and A. Virdis, "Assessment and pathophysiology of microvascular disease: recent progress and clinical implications," European Heart Journal, vol. 42, no. 26, pp. 2590–2604, 11 2020.

[11] M. Roustit and J.-L. Cracowski, "Non-invasive assessment of skin microvascular function in humans: An insight into methods," Microcirculation, vol. 19, no. 1, pp. 47–64, 2012.

[12] N. Benjamin, A. Calver, J. Collier, B. Robinson, P. Vallance, and D. Webb, "Measuring forearm blood flow and interpreting the responses to drugs and mediators," Hypertension, vol. 25, no. 5, pp. 918–923, 1995.

[13] M. Hedetoft and N. V. Olsen, "Evaluation of endothelial function by peripheral arterial tonometry and relation with the nitric oxide pathway," Nitric Oxide, vol. 42, pp. 1–8, 2014.

[14] T. Panula, T. Koivisto, M. Pänkäälä, T. Niiranen, I. Kantola, and M. Kaisti, "An instrument for measuring blood pressure and assessing cardiovascular health from the fingertip," Biosensors and Bioelectronics, vol. 167, p. 112483, 2020.

[15] C. F. Babbs, "Oscillometric measurement of systolic and diastolic blood pressures validated in a physiologic mathematical model," BioMedical Engineering OnLine, vol. 11, no. 1, p. 56, Aug 2012.

[16] K. Yamakoshi, H. Shimazu, M. Shibata, and A. Kamiya, "New oscillometric method for indirect measurement of systolic and mean arterial pressure in the human finger. part 2: correlation study," Medical and Biological Engineering and Computing, vol. 20, no. 3, pp. 314–318, May 1982.

[17] J. Allen, "Photoplethysmography and its application in clinical physiological measurement," Physiological Measurement, vol. 28, no. 3, pp. R1–R39, feb 2007.

[18] D. Ray, T. Collins, S. Woolley, and P. Ponnapalli, "A review of wearable multi-wavelength photoplethysmography," IEEE Reviews in Biomedical Engineering, vol. PP, pp. 1–1, 2021.

[19] J. Liu, B. Yan, S.-C. Chen, Y.-T. Zhang, C. Sodini, and N. Zhao, "Non-invasive capillary blood pressure measurement enabling early detection and classification of venous congestion," IEEE Journal of Biomedical and Health Informatics, vol. 25, no. 8, pp. 2877–2886, 2021.

[20] J.-P. Sirkiä, T. Panula, and M. Kaisti, "The effects of external pressure on multi-wavelength photoplethysmography signals," in 2021 Computing in Cardiology (CinC), vol. 48, 2021, pp. 1–4.

[21] W. J. Bos, E. Verrij, H. H. Vincent, B. E. Westerhof, G. Parati, and

G. A. van Montfrans, "How to assess mean blood pressure properly at the brachial artery level," Journal of Hypertension, vol. 25, no. 4, 2007.
[22] F. Scholkmann, J. Boss, and M. Wolf, "An efficient algorithm for automatic peak detection in noisy periodic and quasi-periodic signals," Algorithms, vol. 5, no. 4, pp. 588–603, 2012.
[23] I. M. Braverman, "The cutaneous microcirculation," Journal of Investigative Dermatology Symposium Proceedings, vol. 5, no. 1, pp. 3–9, 2000.
[24] S. Prahl, M. Keijzer, S. Jacques, and A. Welch, "A monte carlo model of light propagation in tissue," SPIE Inst. Ser. IS, vol. 5, 01 1989.
[25] S. L. Jacques and L. Wang, Monte Carlo Modeling of Light Transport in Tissues. Boston, MA: Springer US, 1995, pp. 73–100.
[26] L. Wang, S. L. Jacques, and L. Zheng, "Mcml—monte carlo modeling of light transport in multi-layered tissues," Computer Methods and Programs in Biomedicine, vol. 47, no. 2, pp. 131–146, 1995.
[27] T. Pfefer, J. Kehlet Barton, E. Chan, M. Ducros, B. Sorg, T. Milner, J. Nelson, and A. Welch, "A three-dimensional modular adaptable grid numerical model for light propagation during laser irradiation of skin tissue," IEEE Journal of Selected Topics in Quantum Electronics, vol. 2, no. 4, pp. 934–942, 1996.
[28] D. A. Boas, J. P. Culver, J. J. Stott, and A. K. Dunn, "Three dimensional monte carlo code for photon migration through complex heterogeneous media including the adult human head," Opt. Express, vol. 10, no. 3, pp. 159–170, Feb 2002.
[29] J. Liu, C. G. Sodini, Y. Ou, B. Yan, Y.-T. Zhang, and N. Zhao, "Feasibility of fingertip oscillometric blood pressure measurement: Model-based analysis and experimental validation," IEEE Journal of Biomedical and Health Informatics, vol. 24, no. 2, pp. 533–542, 2020.
[30] G. Tusman, C. M. Acosta, S. Pulletz, S. H. Böhm, A. Scandurra, J. M. Arca, M. Madorno, and F. S. Sipmann, "Photoplethysmographic characterization of vascular tone mediated changes in arterial pressure: an observational study," Journal of Clinical Monitoring and Computing, vol. 33, no. 5, pp. 815–824, Oct 2019.
[31] H. Njoum and P. A. Kyriacou, "Investigation of finger reflectance photoplethysmography in volunteers undergoing a local sympathetic stimulation," Journal of Physics: Conference Series, vol. 450, p. 012012, jun 2013.
[32] A. Chandrasekhar, C.-S. Kim, M. Naji, K. Natarajan, J.-O. Hahn, and R. Mukkamala, "Smartphone-based blood pressure monitoring via the oscillometric finger-pressing method," Science Translational Medicine, vol. 10, no. 431, p. eaap8674, 2018.
[33] S. Lammers, D. Scott, K. Hunter, W. Tan, R. Shandas, and K. R. Stenmark, Mechanics and Function of the Pulmonary Vasculature: Implications for Pulmonary Vascular Disease and Right Ventricular Function. John Wiley & Sons, Ltd, 2012, pp. 295–319.
[34] S. A. Williams, S. Wasserman, D. W. Rawlinson, R. I. Kitney, L. H. Smaje, and J. E. Tooke, "Dynamic measurement of human capillary blood pressure," Clinical Science, vol. 74, no. 5, pp. 507–512, 05 1988.
[35] A. C. Shore, D. D. Sandeman, and J. E. Tooke, "Capillary pressure, pulse pressure amplitude, and pressure waveform in healthy volunteers," American Journal of Physiology-Heart and Circulatory Physiology, vol. 268, no. 1, pp. H147–H154, 1995.
[36] A. C. Shore, "Capillaroscopy and the measurement of capillary pressure," British Journal of Clinical Pharmacology, vol. 50, no. 6, pp. 501–513, 2000.
[37] M. Hahn, T. Klyscz, and M. Jünger, "Synchronous measurements of blood pressure and red blood cell velocity in capillaries of human skin," Journal of Investigative Dermatology, vol. 106, no. 6, pp. 1256–1259, 1996.
[38] P. Abraham, B. Fromy, S. Merzeau, A. Jardel, and J.-L. Saumet, "Dynamics of local pressure-induced cutaneous vasodilation in the human hand," Microvascular Research, vol. 61, no. 1, pp. 122–129, 2001.
[39] M. Fouchard, L. Misery, R. Le Garrec, D. Sigaudo-Roussel, and B. Fromy, "Alteration of Pressure-Induced Vasodilation in Aging and Diabetes, a Neuro-Vascular Damage," Front Physiol, vol. 10, p. 862, 2019.
[40] A. Koïtka, P. Abraham, B. Bouhanick, D. Sigaudo-Roussel, C. Demiot, and J. L. Saumet, "Impaired Pressure-Induced Vasodilation at the Foot in Young Adults With Type 1 Diabetes," Diabetes, vol. 53, no. 3, pp. 721–725, 03 2004.
[41] J. Vouillarmet, A. Josset-Lamaugarny, P. Michon, J. L. Saumet, A. Koitka-Weber, S. Henni, B. Fromy, and D. Sigaudo-Roussel, "Neurovascular Response to Pressure in Patients With Diabetic Foot Ulcer," Diabetes, vol. 68, no. 4, pp. 832–836, 01 2019.
[42] T. Kuznetsova, E. V. Vlierberghe, J. Knez, G. Szczesny, L. Thijs, D. Jozeau, C. Balestra, J. D'hooge, and J. A. Staessen, "Association of digital vascular function with cardiovascular risk factors: A population study," BMJ Open, vol. 4, no. 3, p. e004399, Mar. 2014.
[43] S. Laurent, C. Agabiti-Rosei, R. M. Bruno, and D. Rizzoni, "Microcirculation and macrocirculation in hypertension: A dangerous cross-link?" Hypertension, vol. 79, no. 3, pp. 479–490, 2022.
[44] S. Chatterjee, K. Budidha, and P. A. Kyriacou, "Investigating the origin of photoplethysmography using a multiwavelength monte carlo model," Physiological Measurement, vol. 41, no. 8, p. 084001, sep 2020.
[45] J. Nijboer and J. Dorlas, "The origin of inverted waveforms in the reflection plethysmogram," British Journal of Anaesthesia, vol. 54, no. 12, pp. 1289–1293, 1982.
[46] T. Li, H. Gong, and Q. Luo, "Mcvm: Monte carlo modeling of photon migration in voxelized media," Journal of Innovative Optical Health Sciences, vol. 03, no. 02, pp. 91–102, Apr. 2010.
[47] O. Kim, J. McMurdy, C. Lines, S. Duffy, G. Crawford, and M. Alber, "Reflectance spectrometry of normal and bruised human skins: Experiments and modeling," Physiological measurement, vol. 33, pp. 159–75, 02 2012.
[48] N. Bosschaart, G. Edelman, M. Aalders, T. van Leeuwen, and D. Faber, "A literature review and novel theoretical approach on the optical properties of whole blood," Lasers in medical science, vol. 29, 10 2013.
[49] I. Meglinski and S. Matcher, "Computer simulation of the skin reflectance spectra," Computer Methods and Programs in Biomedicine, vol. 70, no. 2, pp. 179–186, 2003.
[50] R. Dolenec, E. Laistler, and M. Milanic, "Assessing spectral imaging of the human finger for detection of arthritis," Biomedical optics express, vol. 10, no. 12, pp. 6555–6568, Nov 2019.
[51] A. Bashkatov, E. Genina, V. Tuchin, G. Altshuler, and I. Yaroslavsky, "Monte carlo study of skin optical clearing to enhance light penetration in the tissue: implications for photodynamic therapy of acne vulgaris (proceedings paper)," Proceedings of SPIE - The International Society for Optical Engineering, vol. 7022, 06 2008.
[52] H. Fruhstorfer, U. Abel, C.-D. Garthe, and A. Knüttel, "Thickness of the stratum corneum of the volar fingertips," Clinical Anatomy, vol. 13, no. 6, pp. 429–433, 2000.
[53] X. Liu, Z. Lu, R. Lewis, M. Carré, and S. Matcher, "Feasibility of using optical coherence tomography to study the influence of skin structure on finger friction," Tribology International, vol. 63, pp. 34–44, 2013, the International Conference on BioTribology 2011.
[54] R. A. Hicklin, Anatomy of Friction Ridge Skin. Boston, MA: Springer US, 2009, pp. 23–28.
[55] A. E. Karsten and J. E. Smit, "Modeling and verification of melanin concentration on human skin type," Photochemistry and Photobiology, vol. 88, no. 2, pp. 469–474, 2012.
[56] B. Strauch and W. de Moura, "Arterial system of the fingers," The Journal of Hand Surgery, vol. 15, no. 1, pp. 148–154, 1990.
[57] E. Laistler, B. Dymerska, J. Sieg, S. Goluch, R. Frass-Kriegl, A. Kuehne, and E. Moser, "In vivo mri of the human finger at 7 t," Magnetic Resonance in Medicine, vol. 79, no. 1, pp. 588–592, 2018.